ACS OMEGA

http://pubs.acs.org/journal/acsodf

Article

Separation of Etiracetam Enantiomers Using Enantiospecific Cocrystallization with 2-Chloromandelic Acid

Thitapond Nulek, Rachan Klaysri, Ruel Cedeno, Phattananawee Nalaoh, Sareeya Bureekaew, Vinich Promarak, and Adrian E. Flood*

Cite This: *ACS Omega* 2022, 7, 19465−19473

Read Online

ACCESS | Metrics & More | Article Recommendations | Supporting Information

ABSTRACT: Chirality plays an important role in the pharmaceutical industry since the two enantiomers of a drug molecule usually display significantly different bioactivities, and hence, most products are produced as pure enantiomers. However, many drug precursors are synthesized as racemates, and hence, enantioseparation has become a significant process in the industry. Cocrystallization is one of the attractive crystallization approaches to obtain the desired enantiomer from racemic compounds. In this work, we propose a chiral resolution route for an antiepileptic drug, *S*-etiracetam (*S*-ETI), via enantiospecific cocrystallization with *S*-2-chloro-*S*-mandelic acid (CLMA) as a coformer. The experiments indicate that the system is highly enantiospecific; *S*-2CLMA cocrystallizes only with *S*-ETI but not with *R*-ETI or *RS*-ETI. Therefore, the chiral purification of *S*-ETI can be achieved efficiently with a 69.1% yield and close to 100% enantiopurity from the racemic solution. Additionally, structural simulations of the *S*-ETI:*S*-2CLMA cocrystal reveal that the cocrystal structure has higher thermodynamic stability than that of *R*-ETI:*S*-2CLMA by about 5.5 kcal/mol (per cocrystal formula unit), which helps to confirm the favorability of the enantiospecification in this system.

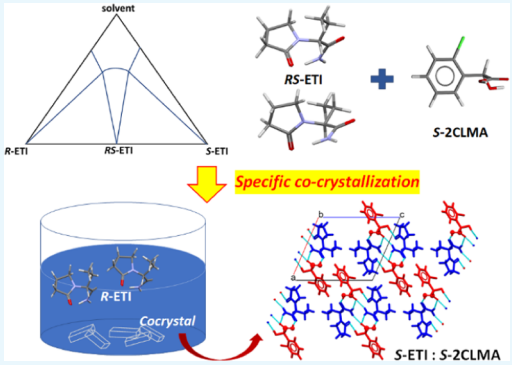

1. INTRODUCTION

Enantioseparation processes are a crucial step in the pharmaceutical industry since new active pharmaceutical ingredients (APIs) are required to have high enantiopurity due to the possible adverse side effects of the undesired enantiomer.[1] Preferential crystallization has been an easy and very effective method to separate the desired enantiomer from the undesired one.[2,3] Unfortunately, this technique requires enantiomers to crystallize as a conglomerate-forming system, which is only found in ∼5−10% of all chiral systems.[4] Thus, diastereomeric salt formation is still widely used in the industry because it can be used with racemates, which are 90−95% of chiral crystalline compounds.[4,5]

An alternative chiral resolution method, cocrystallization using a chiral coformer, has been proposed for nonionizable compounds, especially racemates, that cannot easily form a salt.[6] Enantiospecific cocrystallization was first introduced by Springuel and Leyssens.[7] In this process, the coformer only cocrystallizes with one of the two enantiomers of the API, and the process can be performed with high enantiopurity and yield. However, the separation also can be done by diastereomeric cocrystallization, in which the coformer interacts with both enantiomers. Obviously, enantiospecific cocrystallization is more attractive since it is easier to design the crystallization process as the number of solid phases in the phase diagram is reduced.[8] Even though chiral resolution via cocrystallization has a common principle with the diastereomeric salt formation technique, adding another chiral compound to form a new crystalline product with a specific enantiomer, the mechanism and outcome are very different. The cocrystallization technique relies on intermolecular interactions between the API and coformer, such as hydrogen bonding, halogen bonding, CH−π interactions,[9] and van der Waals forces.[8] In diastereomeric salt formation, the API and resolving agent interact via strong ionic bonds.[8] Therefore, enantiopurification via cocrystallization is a worthwhile approach for resolution of racemic mixtures since the cocrystal formation does not alter the speciation of the compound in the crystallization step, maintaining its biological activity.[6] Another significant difference between these two procedures is that the cocrystallization technique commonly behaves as an enantiospecific system,[7,8,10,11] in contrast with salt formation where both diastereomers can form but one is typically more stable than the other.[8] Moreover, the hydrogen bonding pattern in cocrystals tends to be weaker and far more directional and thus

Received: February 26, 2022
Accepted: May 16, 2022
Published: June 2, 2022

ACS Publications

© 2022 The Authors. Published by American Chemical Society

dependent on the stereochemistry of the API than the ionic bond in salt formation.[8] Lastly, the separation process of cocrystals is much easier than that in salt formation because of the weaker bonds involved in cocrystals.

Levetiracetam or *S*-2-(2-oxopyrrolidin-1-yl)butanamide is an antiepileptic drug sold under the name Keppra. It is used for treating the symptoms of epileptic seizures that can also occur with patients who have primary or secondary tumors;[12] however, there is no report on the pharmaceutical efficacy of its enantiomer, *R*-etiracetam (*R*-ETI).[13] Furthermore, *S*-etiracetam (*S*-ETI) is also used in combination with other medicines to treat individual types of seizures.[14] Naturally, *S*-ETI is a chiral drug that crystallizes as a racemic compound rather than as a conglomerate. Consequently, direct preferential crystallization is expected to be difficult to apply to this system unless a convenient conglomerate salt or derivative can be found. Springuel and Leyssens have successfully resolved *S*-ETI from its racemic mixture with 70% yield using *S*-mandelic acid as a coformer via enantiospecific cocrystallization.[7] Cocrystallization using *S*-ibuprofen has also resolved *S*-ETI from its racemic mixture with 87.6% ee.[10] In another study, the racemate is converted to an ionic cocrystal by adding a suitable amount of $ZnCl_2$ to the etiracetam solution, which then facilitates chiral resolution.[15] In addition, cocrystals of *S*-ETI with other compounds have also been found, with coformers including *R*-α-ketoglutaric acid[11] and D-tartaric acid.[16] Recently, enantioseparation has been achieved for a range of halogenated mandelic acids using cocrystallization with levetiracetam as a resolving agent.[17] Although one of the two diastereomers involved in the separation of the halogenated mandelic acid enantiomers will be similar to that used in the separation of the levetiracetam enantiomers, the potential second diastereomeric cocrystal in the two cases is distinct, which means that the ability to use enantioseparation in the first case does not indicate that the second case will also be successful. This led to a question whether halogenated mandelic acids could be a viable resolving agent for the enantiopurification of levetiracetam.

In cocrystallization, although there are heuristic rules for selecting suitable coformers,[18] the screening process is still generally done via a trial-and-error approach. This shows that further understanding of the molecular origins governing the chiral discrimination mechanism in cocrystal systems is needed. Thus, the purposes of this study are discovering a new chiral cocrystal system and performing chiral resolution via cocrystallization. Moreover, the study aims to gain further understanding of the molecular origins governing the chiral discrimination mechanism in this cocrystal system.

In this work, we demonstrate an enantiopurification route for *RS*-ETI using the chiral coformer 2-chloro-*S*-mandelic acid (*S*-2CLMA), an important cardiovascular drug precursor.[19] Characterizations of the new cocrystal and chiral resolution via the cocrystallization technique are illustrated in this paper. In addition, we elucidate for the first time the crystal structure of this chiral cocrystal by X-ray crystallography and analyze the intermolecular interactions via density functional theory (DFT) calculations to gain more insights into the observed enantiospecific behavior. The techniques and insights presented here could be useful to guide the design of enantiospecific cocrystallization and obtain an idea for screening of suitable coformers.

2. MATERIALS

2.1. Starting Materials. 2-Chloro-*S*-mandelic acid (*S*-2CLMA) and 2-chloro-*R*-mandelic acid (*R*-2CLMA) were purchased from TCI with a purity of >98%. Racemic etiracetam (*RS*-ETI) was obtained by racemization of *S*-ETI purchased from Acros following a procedure similar to that of Springuel et al.[20] Starting with 2 g of levetiracetam, 0.05 equiv of sodium methoxide was added to 2 mL of methanol. The solution was stirred at 50 °C for 24 h using a condenser to return any solvent that evaporated. Then, the solution was cooled in a bath at 5 °C to let the compound crystallize. The solid phase was filtered and washed with cold methanol before drying in a vacuum oven. HPLC and NMR were used to confirm that complete racemization had occurred with no degradation of the etiracetam. Deionized (DI) water (PURELAB Classic, 15.0 MΩ cm, type II) and acetonitrile (Honeywell, HPLC grade) were used as solvents without further purification.

2.2. Screening Experiment. Screening experiments of two API compounds, *S*-ETI and *RS*-oxiracetam, were done with various coformers using the neat grinding technique. An equimolar ratio of the mentioned APIs with various coformers was ground for either 2 or 3 h; then, the solid was characterized by XRPD. The pairs that have been examined are given in Table S1.

2.3. Liquid-Assisted Grinding for Cocrystal Creation. The cocrystal for characterization of the stable form was prepared using a liquid-assisted grinding technique with an equimolar ratio of *S*-ETI and *S*-2CLMA in the presence of a small amount of acetonitrile. In the experiment, 0.268 mmol *S*-2CLMA and *S*-ETI were mixed in a grinding tube with an addition of 10 μL of acetonitrile and two milling balls (7 mm diameter). The mixture was then ground using a Retsch MM200 ball mill at a frequency of 25 rounds/s for 60 min. Then, the solid was dried and characterized by XRPD and TGA.

2.4. Single Crystal of the Levetiracetam-2-Chloro-*S*-Mandelic Acid Cocrystal. A total of 0.2 g of *S*-ETI:*S*-2CLMA cocrystal from multiple cocrystal preparations was dissolved in 1 mL of chloroform (boiling point of 61.2 °C). After the cocrystal was completely dissolved, 1 mL of hexane (boiling point of 69 °C) was added as an antisolvent. Then, the vial was left under stirring under ambient conditions with the cap loosened to allow the solvents to slowly evaporate. Since the chloroform solvent has a lower boiling point than that of the antisolvent hexane, the molar ratio of the antisolvent to the solvent increased during the evaporation process. Single crystals formed after some of the solvent mixture evaporated. Finally, a single crystal suitable for X-ray crystallography was obtained.

2.5. Chiral Resolution. A total of 114 mg of racemic ETI was mixed with *S*-2CLMA in 1:1 mole ratio. Then, the solid mixture was dissolved in 0.5 mL of acetonitrile at 65 °C for 35 min. After the suspension was completely dissolved, the solution was cooled to −14 °C. The *S*-ETI:*S*-2CLMA cocrystal from liquid-assisted grinding was seeded into the vial after the solution reached the crystallization temperature. A cocrystal formed immediately after seeding, but to get a satisfying yield, the crystalline solid was collected 48 h after seeding. Then, the crystalline solid was washed with 2 mL of cooled diethyl ether and dried at 40 °C under vacuum. To analyze the enantiomeric excess and yield of the resolved enantiomer (*S*-ETI), 1 mg of

https://doi.org/10.1021/acsomega.2c01165
ACS Omega 2022, 7, 19465−19473

the cocrystal was stirred for 1 h in 150 μL of diethyl ether, which is an appropriate amount of solvent to dissolve most of the *S*-2CLMA from the cocrystal while obtaining a good yield of *S*-ETI (Table S2). Diethyl ether was chosen as the solvent for this process since the solubility of *S*-ETI in this solvent is very low (less than 0.007 g/g of diethyl ether[21]) compared to the solubility of *S*-2CLMA (0.369 g/g of diethyl ether[22]), which makes it suitable for separating the components of the cocrystal. The solubilities of the components in other solvents that were considered are shown in the Supporting Information, Table S3. Afterward, the remaining solid was filtered and analyzed by HPLC using a Chiralcel OD column. Details of the HPLC technique are given in the Supporting Information.

2.6. Computational Details. For solid-state simulations, we used the experimental crystal structure of *S*-ETI:*S*-2CLMA determined in this work as a starting geometry. To explain why *R*-ETI:*S*-2CLMA is not observed experimentally, we employed crystal structure prediction (CSP) to scan its energy landscape via a quasi-random search.[23] To reduce the number of trial structures, we used a Monte Carlo procedure to preliminarily screen low-energy interacting pairs (synthons) using the Gmmx[24] module as implemented in PCModel v10.[25] The structures were then optimized using the Merck molecular force field (MMFF94).[26] The search is stopped when the maximum number of randomly generated synthons reaches 10 000 or when at least one pair reaches 50 duplicates. The 10 most stable synthons were used as the initial asymmetric unit. To generate random unit cells with a predefined space group, we used the Pyxtal program.[27] We constrained the initial cell volume per asymmetric unit to be comparable to that of the *S*-ETI:*S*-2CLMA cocrystal. To reduce the computational cost, we constrained the search space to the most common space groups for chiral cocrystals,[28] i.e., *P*1, *P*-1, P2, *P*21, *P*21/*c*, and *P*212121. The generated unit cells were then optimized using the semiempirical PM7 Hamiltonian with periodic boundary conditions as implemented in MOPAC v2016,[29,30] which has been shown to have good performance in predicting thermodynamic properties particularly for organic systems.[31,32] The structures of the five most stable candidates were further refined using periodic density functional theory (DFT) calculations as implemented in the CP2K package,[33] which uses a mixed Gaussian/plane-wave (GPW) basis set. The exchange and correlation energies were evaluated using the semilocal Perdew−Burke−Ernzerhof (PBE) form of the generalized gradient approximation (GGA) functional together with Grimme's D3 van der Waals correction.[34,35] DZVP-MOLOPT basis sets and Goedecker−Teter−Hutter (GTH) pseudopotentials were selected in the calculations.[36,37] An energy cutoff of 500 Ry and relative energy cutoff of 80 Ry were found to be sufficient for energy convergence. Brillouin zone integration was sampled at the Γ point, which is sufficient due to the large size of the supercell (1 × 2 × 1 cell containing 180 atoms). Atomic structures were optimized using the BFGS algorithm[38] until the forces acting on each atom were less than 0.005 eV/Å. For self-consistent total energy calculations, the convergence criterion was set to 10^{-7} Hartrees for the crystal structure's full relaxation (lattice and atomic position optimizations). To evaluate the thermal contributions to the enthalpy and free energy, we performed vibrational frequency analysis at the DFT-D3/revPBE/DZVP level of theory under harmonic approximation. The thermodynamic properties were then computed using the postprocessing tool TAMkin.[39]

3. RESULTS AND DISCUSSION

3.1. Screening and Characterization. We have screened various resolving agents that could form enantiospecific cocrystals with *S*-ETI via grinding experiments (details shown in Table S1). We found that *S*-ETI forms a cocrystal with *S*-2CLMA but not with *R*-2CLMA. This is evidenced by the XRPD pattern shown in Figure 1a. The powder pattern of

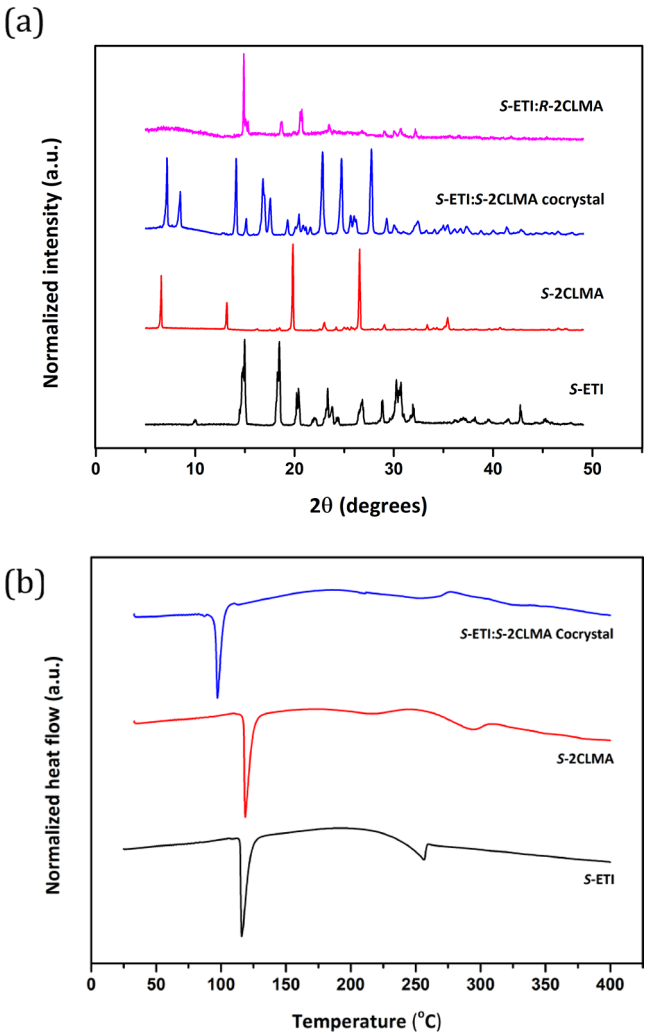

Figure 1. (a) Powder X-ray diffraction patterns of *S*-ETI, *S*-2CLMA, and *S*-ETI:*S*-2CLMA cocrystals and *S*-ETI:*R*-2CLMA. (b) Melting temperatures of *S*-ETI, *S*-2CLMA, and *S*-ETI:*S*-2CLMA cocrystals with 5 °C/min heating rate.

S-ETI:*S*-2CLMA is significantly different from that of *S*-ETI and *S*-2CLMA, suggesting the formation of a new crystalline phase. On the other hand, the powder pattern of *S*-ETI:*R*-2ClMA is comparable to that of S-ETI. Notice that the peaks corresponding to *R*-2CLMA disappeared. This is likely due to transformation into an amorphous phase due to the excess energy produced or the increase in temperature during the grinding experiment.[40,41] Nevertheless, this confirms that *S*-ETI:*R*-2CLMA is an enantiospecific cocrystal. To further confirm this, we performed thermogravimetric analysis whose results are shown in Figure 1b. Pure *S*-2CLMA and *S*-ETI have similar melting temperatures, 119 and 117 °C, respectively, whereas the cocrystal has a melting point of 98 °C, thereby confirming the formation of a new phase.

https://doi.org/10.1021/acsomega.2c01165
ACS Omega 2022, 7, 19465−19473

3.2. Crystal Structure Analysis. To elucidate the crystal structure of *S*-ETI:*S*-2CLMA, we performed single-crystal X-ray crystallography. To the best of our knowledge, this is the first time that the crystal structure of this cocrystal has been determined. The pertinent crystallographic data in Table 1 show that *S*-ETI:*R*-2CLMA crystallizes in the monoclinic $P2_1$ space group. Moreover, the simulated peaks obtained from the single crystal exhibit excellent correlation with the experimental powder pattern (Figure S2). This suggests that the bulk powder obtained by batch crystallization is well-represented by the selected single crystal, thus ruling out the presence of other phases or polymorphs in the system. Furthermore, given that the system is enantiospecific, it is expected that the counter-enantiomer (*R*-ETI:*R*-2CLMA) would have a similar structure by virtue of symmetry.

Table 1. Crystallographic Data and Refinement Details of the *S*-ETI:*S*-2CLMA Cocrystal

crystal data	
chemical formula	$C_{16}H_{21}ClN_2O_5$
M_r	356.8
temperature (K)	100
crystal system	monoclinic
space group	$P2_1$
a, b, c (Å)	11.6912 (7), 5.7422 (4), 13.8421 (9)
α, β, γ (deg)	90, 113.527 (2), 90
V (Å^3)	852.02 (10)
Z	2
F (000)	376
density calculated (g/cm^3)	1.391
radiation type	Mo Kα (λ = 0.71073)
μ (mm^{-1})	0.253
crystal size (mm^3)	0.62 × 0.19 × 0.08
data collection	
diffractometer	Bruker D8 Venture
absorption correction	multiscan (SADABS; Bruker, 2016)
T_{min}, T_{max}	0.681, 0.746
R_{int}	0.0325
refinement	
goodness-of-fit on F^2	1.057
R_1, wR_2 [$I > = 2\sigma I$]	0.028, 0.0688
R_1, wR_2 [all data]	0.0322, 0.0707
no. of reflections	17 385
no. of parameters	222
$\Delta\rho_{max}$, $\Delta\rho_{min}$ (e Å^{-3})	0.38, −0.21
Flack value	0.041

To understand the underlying intermolecular interactions that stabilize the cocrystal, we further examined its crystal structure. The asymmetric unit in Figure 2a shows a ring-like $R_2^2(8)$ H-bonding motif between *S*-ETI and *S*-2CLMA. This motif is visible in the crystal packing along the ac-plane (Figure 2b) where *S*-ETI is shown in red and *S*-2CLMA is shown in blue. The perspective view along the same plane (Figure 2c) reveals that this ring-like motif propagates along the *b*-direction, which is affirmed by the crystal packing along the ab-plane exhibiting an infinite chain of H-bond network. Analysis of the geometric parameters reveals four important intermolecular H-bonding interactions reported in Table S4. The strongest of these is the 1.77 Å bond between the carboxylic hydrogen of *S*-2CLMA and the amide oxygen of *S*-ETI (Figure 2d). This is followed by the 1.99 Å bond between the hydroxyl hydrogen of *S*-2CLMA and pyrrolidone oxygen of *S*-ETI. The remaining H-bonds are due to the interaction between the amide of the *S*-ETI and the carboxylic oxygen of the *S*-2CLMA.

3.3. Molecular Simulations. To understand why this cocrystal system behaves enantiospecifically, we generated and ranked the most probable crystal structure of *R*-ETI:*S*-2CLMA (the less-stable diastereomeric cocrystal) via molecular simulations, constrained within the most common space groups for chiral cocrystals (i.e., $P1$, $P\bar{1}$, $P2$, $P2_1$, $P2_1/c$, and $P2_12_12_1$).[28] The resulting energy landscape is reported in Figure 3. For comparison, the experimental crystal structures of enantiopure ETI, *rac*-ETI, *S*-2CLMA, and *S*-ETI:*S*-2CLMA are included. From a thermodynamic perspective, a cocrystal would likely form if its lattice energy is larger in magnitude than the sum of the lattice energies of the coformers (the gray line in Figure 3). Interestingly, two of the predicted structures satisfy this threshold and are energetically close to the experimental *S*-ETI:*S*-2CLMA form (with around 2 and 4 kcal/mol difference, respectively, at the PM7 level of theory).

To refine the structure of the most stable hypothetical structure, we further relaxed its structure at the DFT-D3/revPBE/DZVP level of theory with periodic boundary conditions. Note that the dispersion-corrected DFT is generally considered more accurate than semiempirical PM7 but comes with a greater computational cost. The resulting hypothetical structure in comparison with the DFT-optimized experimental structure of the other stereoisomer is shown in Figure 4. Moreover, the two crystal structures are remarkably similar as evidenced by the resemblance of their simulated powder pattern (Figure S3).

To evaluate the stabilities of the crystal structures at various temperatures, we performed vibrational analysis at the DFT-D3/revPBE/DZVP level of theory together with harmonic approximation. The difference in enthalpy ΔH and free energy ΔG between the predicted hypothetical structure (*R*-ETI:*S*-2CLMA) and the experimental structure (*S*-ETI:*S*-2CLMA) is reported in Figure S4. Interestingly, although the two crystal structures are remarkably similar, their stabilities are markedly different. At the selected temperature range, ΔH remains relatively constant at around −5.5 kcal/mol, which confirms that the experimentally observed cocrystal has stronger bond energies. The flat variation of ΔH with temperature suggests that the two cocrystals have similar specific heat capacities. On the other hand, ΔG is negative and increases with temperature, implying that the hypothetical structure is entropically favored (more disordered).

Consequently, the two cocrystals would have a closer magnitude of free energy at higher temperatures (below the melting point). This supports the idea that the strength of stereospecific interactions is highly directional; thus, such interactions would diminish when molecular vibration increases.

With such a difference in stability despite having a similar crystal packing, one might expect that the H-bond interaction distances of the predicted *R*-ETI:*S*-2CLMA cocrystal must be systematically longer than those of the stable *S*-ETI:*S*-2CLMA cocrystal. However, as shown in Figure 4, this is not the case, as some H-bonds of the unstable cocrystal are shorter. To further investigate this, we employed the Hirshfeld surface analysis, which is a popular approach to quantify differences in intermolecular interactions as implemented in CrystalExplorer.[42] The Hirshfeld surface can be defined as a region of space

https://doi.org/10.1021/acsomega.2c01165
ACS Omega 2022, 7, 19465−19473

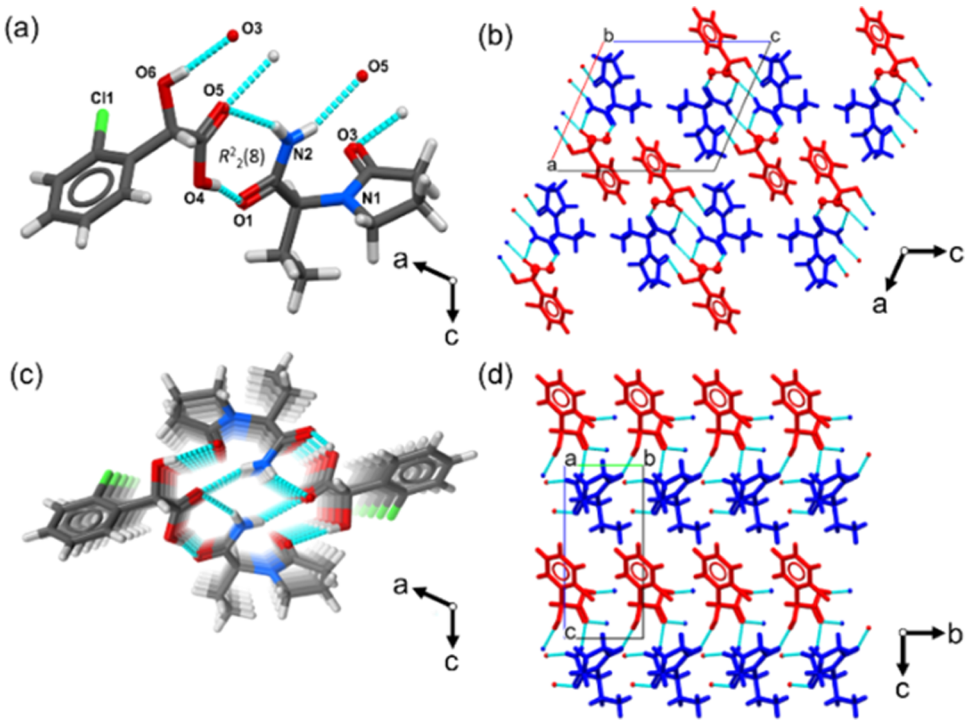

Figure 2. (a) Asymmetric unit of the *S*-ETI:*S*-2CLMA cocrystal; (b) packing along the *ac*-plane; (c) perspective view along the *ac*-plane; and (d) packing along the *bc*-plane.

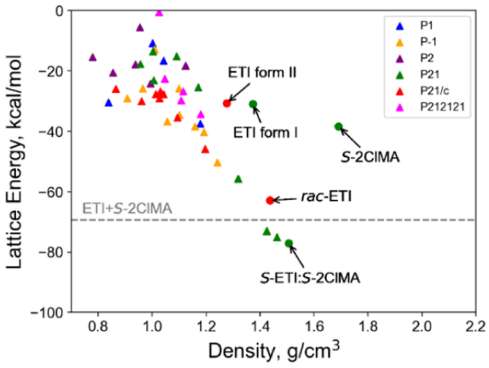

Figure 3. Energy landscape of the predicted crystal structures of *R*-ETI:*S*-2CLMA (in ▲) in comparison with experimental crystal structures (in ●) computed at the semiempirical PM7 level of theory (at 25 °C, 1 bar). The critical lattice energy (gray dashed line) is set as the sum of the conformer's lattice energy (enantiopure ETI plus *S*-2CLMA). The color corresponds to the space group.

surrounding a particular molecule where its contribution to the total electron density is equal to that of its surroundings.[43] Intermolecular interactions can then be visualized by mapping the color of the surface with the normalized contact distance, d_{norm}, which compares the distance between two atoms across the surface to the combined van der Waals radii of the atoms.

The Hirshfeld surfaces of both cocrystals are shown in Figure 5a,b, and the corresponding fingerprint plots are shown in Figure 5c,d (Hirshfeld analysis of each atomic interaction is provided in Figure S5). The conspicuous red regions on the surface (close contacts) are due to O···H contacts, which appear as spikes (encircled in red) in the fingerprint plot. One notable difference between the two fingerprints is the occurrence of a small H···H spike in *R*-ETI:*S*-2CLMA, which does not occur in *S*-ETI: *S*-2CLMA. As a result, the H···H

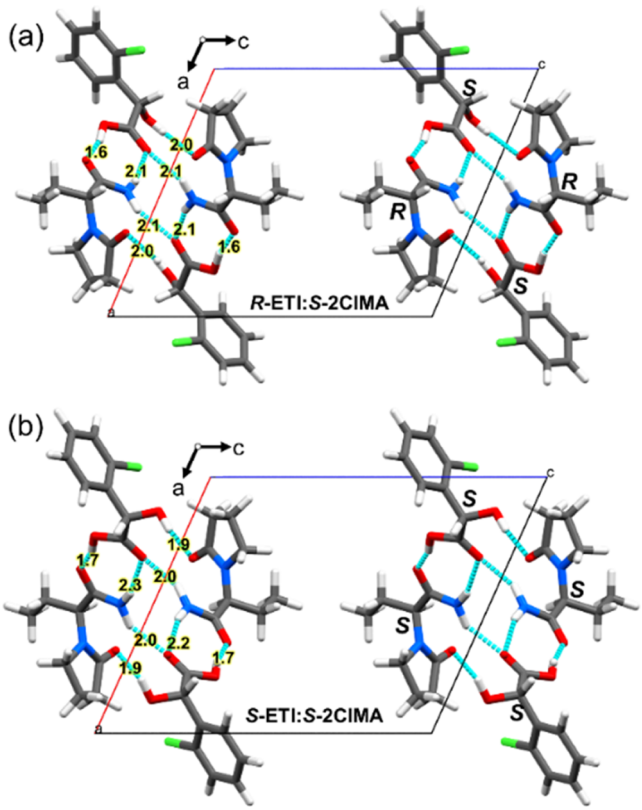

Figure 4. DFT-optimized crystal structures of (a) hypothetical *R*-ETI:*S*-2CLMA and (b) experimental *S*-ETI:*S*-2CLMA. The H-bond lengths (hydrogen to acceptor) are shown in angstroms, and the chiral centers are indicated accordingly.

contribution on the Hirshfeld surface is slightly higher in *R*-ETI: *S*-2CLMA, as shown in Figure 5e, while the others (O···

https://doi.org/10.1021/acsomega.2c01165
ACS Omega 2022, 7, 19465−19473

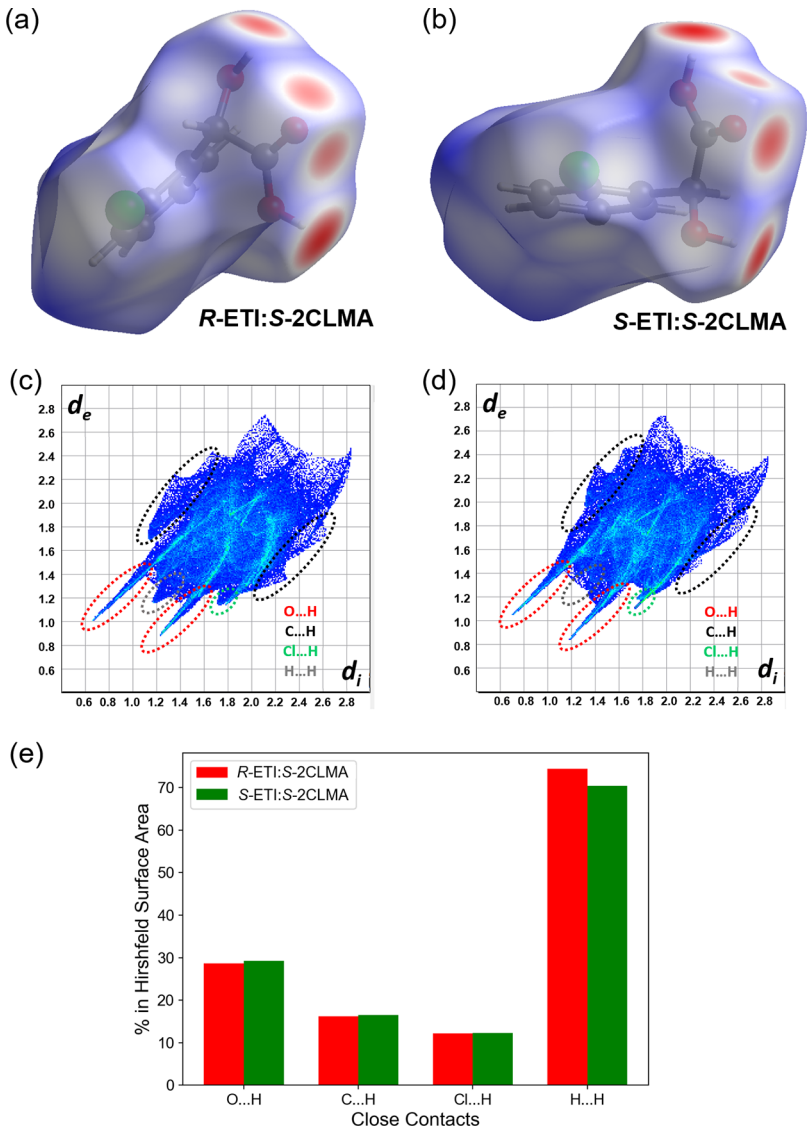

Figure 5. Hirshfeld surfaces of *S*-2CLMA in the cocrystals (a) *R*-ETI:*S*-2CLMA and (b) *S*-ETI:*S*-2CLMA and the corresponding 2D fingerprint plot of (c) *R*-ETI:*S*-2CLMA and (d) *S*-ETI:*S*-2CLMA (interior distance d_i and exterior distance d_e are in angstroms) and (e) comparison of contribution (in %) of selected close contacts to the Hirshfeld surface.

H, C···H, Cl···H) are essentially the same. With this, one might speculate that the H···H repulsion is the reason for the lower stability of *R*-ETI:*S*-2CLMA. However, the sum of d_i and d_e for the closest H···H contact is around 2.4 Å, which is within the range of attractive dispersion interactions for H···H interactions. Thus, this could not explain the observed difference in stability.

Upon further inspection of the structure, we observed that the centroid-to-centroid distance between phenyl rings of *S*-2CLMA is longer in *R*-ETI:*S*-2CLMA than in *S*-ETI:*S*-2CLMA, as shown in Figure 6.

Note that the T-shape aromatic interaction (also known as the edge-to-face interaction) occurs when the distance between the ring centroids is around 5 Å and when the angle between the ring normals is greater than 50°.[44,45] On the other hand, the CH−π interaction occurs when a H attached to C has a distance of less than 3 Å from the aromatic ring centroid.[46] These definitions for T-shape aromatic interactions and CH−π interactions are also consistent with those of the PLATON program.[47] To quantify the strength of the T-shape aromatic

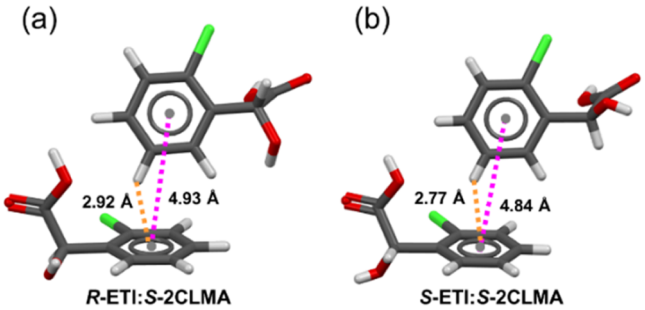

Figure 6. T-shape aromatic interactions (magenta) and CH−π interaction (orange) in (a) *R*-ETI:*S*-2CLMA and (b) *S*-ETI:*S*-2CLMA. The angle between the ring normal is around 71° for both.

interaction, we used the CCDC's *Aromatic Analyzer* as implemented in Mercury,[48] which is based on a neural network model. From the distances between ring centroids and the relative orientation (angle between the ring normals), it calculates an interaction score ranging from 0 (no interaction)

https://doi.org/10.1021/acsomega.2c01165
ACS Omega 2022, 7, 19465−19473

Table 2. Enantiomeric Excess and Experimental Yield of Chiral Resolution Using *S*-2CLMA When Varying the Molar Ratio of *RS*-ETI and *S*-2CLMA

initial composition				final solid composition (HPLC)			
ratio	*RS*-ETI (mg)	*S*-2CLMA (mg)	ACN (mL)	CoCry. weight (mg)	% ee (*S*-ETI)	*S*-ETI[a] (mg)	experimental yield (%) (based on *S*-ETI)
1:1	114	125	0.5	81.5	96.7	39.4	69.1
1:1.5	114	187	0.5	68.0	97.0	36.8	64.6
1:2	114	250	0.5	57.8	98.1	27.0	47.4

[a]The total weight of the cocrystal was measured after washing and drying. The amount of *S*-ETI, *R*-ETI, and %ee was calculated based on the total weight of the cocrystal and ETI composition in the cocrystal by chiral HPLC following eqs 1 and 2.

to 10 (strong interaction). Indeed, the aromatic interaction score of the stable *S*-ETI:*S*-2CLMA is higher than that of the predicted *R*-ETI:*S*-2CLMA cocrystal (Table S5), illustrating the important role of T-shape aromatic interactions and CH−π interactions in the stability of these cocrystals. Thus, we postulate that due to the change in the chirality of ETI in *R*-ETI:*S*-2CLMA, *S*-2CLMA would have to rotate the functional groups attached to its chiral center (−OH and −COOH groups) to maximize the H-bond interactions. However, in the process, the phenyl rings would have to reorient in a way that reduces the strength of T-shape aromatic interactions. This makes the alternative cocrystal less stable as supported by the lower lattice energy. Overall, our simulations reveal molecular-level insights that could rationalize the observed enantiospecific behavior of this cocrystal system.

3.4. Chiral Resolution. Since many polymorphs of racemic ETI[49] have been found, the synthesized *RS*-ETI (form II) that we used in the separation experiment is confirmed by XRPD and NMR, as shown in Figures S6 and S7, respectively. The enantioseparation of *S*-ETI from its racemate was performed in acetonitrile with *S*-2CLMA as a coformer. Enantiomeric excess and yield of the product are defined in eqs 1 and 2, respectively.

$$\text{enantiomeric excess (\%)} = \frac{S - R}{S + R} \times 100\% \quad (1)$$

$$\text{experimental yield} = \frac{S\text{-ETI product}}{\text{initial } S\text{-ETI}} \times 100\% \quad (2)$$

S-ETI:*S*-2CLMA is an incongruent cocrystal system due to the huge differences of the solubility of the two species in acetonitrile. Therefore, an equal ratio of *S*-ETI and *S*-2CLMA is not suitable for the production of the cocrystal. Varying the initial composition ratio between the API and coformer is then vital to obtain the optimum cocrystallization outcome.

Results show that a 1:1 ratio of rac-ETI and *S*-2CLMA is the optimal ratio since the resolution was achieved efficiently with an excellent purity (97% ee) and satisfactory yield (70%) of *S*-ETI, as shown in Table 2. Note that this is a 2:1 ratio of *S*-2CLMA:*S*-ETI. Increasing the amount of *S*-2CLMA further does not improve the experimental yield of *S*-ETI since *S*-2CLMA will crystallize together with the *S*-ETI:*S*-2CLMA cocrystal. This could be explained by a schematic ternary phase diagram, as shown in Figure S8, where the operation conditions exceed the region that allows only the cocrystal to crystallize as a stable phase. Alternatively, reducing the amount of *S*-2CLMA to be 0.5 times by mole of *rac*-ETI (1:1 ratio of cocrystal) is not favorable since only *rac*-ETI was acquired as a solid phase at this point. This is because of the differences in the solubility of *S*-2CLMA that was about 10 times higher than that of *S*-ETI in acetonitrile (Table S3). Therefore, at this ratio, pure *RS*-ETI is the most stable solid phase. Finally, the purity of the desired product (*S*-ETI) in all cases is considerably unchanged because the system is enantiosepecific, which means that only one enantiomer (*S*-ETI) cocrystallizes together with *S*-2CLMA.

4. CONCLUSIONS

In this work, we demonstrate the enantiospecific cocrystallization of etiracetam (ETI) with 2-chloromandelic acid (2-CLMA). In this system, *S*-2CLMA forms a cocrystal with *S*-ETI but not with *R*-ETI. The crystal structure of the new cocrystal has been determined and analyzed. Exploiting the enantiospecific cocrystallization behavior, we showed that the resolution of *S*-ETI from rac-ETI can be achieved efficiently with 96.7% purity and 69.1% yield. To understand why the *R*-ETI:*S*-2CLMA cocrystal does not form, we employed crystal structure prediction and molecular simulations. Although the predicted hypothetical structure of *R*-ETI:*S*-2CLMA is strikingly similar to that of the experimentally observed *R*-ETI:*S*-2CLMA, a large lattice energy difference of 5.5 kcal/mol per cocrystal formula unit was obtained. While both cocrystals have relatively similar H-bonding geometries and Hirshfeld fingerprints, we found that the aromatic interactions in *S*-ETI:*S*-2CLMA are more favorable than in *R*-ETI:*S*-2CLMA, leading to the observed enantiospecific behavior.

For further process design, all compounds in the cocrystallization process could be recycled after the first crystallization stage. In the experiment, *S*-2CLMA can be recycled practicably by washing from the surface of the solid cocrystal with diethyl ether, drying to remove the solvent, and adding back to the reactor, accordingly. For *R*-ETI, racemization could be a process to prepare a racemic solution from the remaining enriched solution and then use it further in the next batch of cocrystallization.

■ ASSOCIATED CONTENT

Supporting Information

The Supporting Information is available free of charge at https://pubs.acs.org/doi/10.1021/acsomega.2c01165.

Screening experiment carried out by grinding; molecular structure of *S*-2-chloromandelic acid and enantiomer of etiracetam; details of characterizations; amounts of DEE used to separate *S*-ETI from the *S*-ETI:*S*-2CLMA cocrystal; solubility of *S*-ETI and *S*-2CLMA in various solvents; characteristic peaks of *the* *S*-ETI:*S*-2CLMA cocrystal from SC-XRD and XRPD; geometric parameters of the intermolecular H-bonds in the *S*-ETI:*S*-2CLMA cocrystal; simulated powder pattern of the predicted structure in comparison with the experimental structure; difference in enthalpy and free energy between the predicted hypothetical structure; aromatic interaction parameters obtained from Aromatics Analyzer of

https://doi.org/10.1021/acsomega.2c01165
ACS Omega 2022, 7, 19465−19473

Mercury; Hirshfeld 2D fingerprint plots; powder X-ray diffraction patterns of *RS*-ETI, *RS*-ETI, and *S*-ETI; ^{13}C NMR of RS-ETI from racemization; and schematic ternary phase diagram of the *S*-ETI:*S*-2CLMA cocrystal in acetonitrile at a particular temperature (PDF)

Accession Codes

The cif file (CCDC code 2092790) contains the supplementary crystallographic data for this paper. These data can also be obtained free of charge via www.ccdc.cam.ac.uk/data_request/cif or by emailing data_request@ccdc.cam.ac.uk or by contacting The Cambridge Crystallographic Data Centre, 12 Union Road, Cambridge CB2 1EZ, UK; Fax: +44 1223 336033.

■ AUTHOR INFORMATION

Corresponding Author

Adrian E. Flood − *Department of Chemical and Biomolecular Engineering, School of Energy Science and Engineering, Vidyasirimedhi Institute of Science and Technology, 21210 Rayong, Thailand;* orcid.org/0000-0003-1691-3085; Email: adrian.flood@vistec.ac.th

Authors

Thitapond Nulek − *Department of Chemical and Biomolecular Engineering, School of Energy Science and Engineering, Vidyasirimedhi Institute of Science and Technology, 21210 Rayong, Thailand*

Rachan Klaysri − *Department of Chemical and Biomolecular Engineering, School of Energy Science and Engineering, Vidyasirimedhi Institute of Science and Technology, 21210 Rayong, Thailand*

Ruel Cedeno − *Department of Chemical and Biomolecular Engineering, School of Energy Science and Engineering, Vidyasirimedhi Institute of Science and Technology, 21210 Rayong, Thailand*

Phattananawee Nalaoh − *Department of Materials Science and Engineering, School of Molecular Science and Engineering, Vidyasirimedhi Institute of Science and Technology, 21210 Rayong, Thailand*

Sareeya Bureekaew − *Department of Chemical and Biomolecular Engineering, School of Energy Science and Engineering, Vidyasirimedhi Institute of Science and Technology, 21210 Rayong, Thailand*

Vinich Promarak − *Department of Materials Science and Engineering, School of Molecular Science and Engineering, Vidyasirimedhi Institute of Science and Technology, 21210 Rayong, Thailand;* orcid.org/0000-0003-4805-9944

Complete contact information is available at: https://pubs.acs.org/10.1021/acsomega.2c01165

Author Contributions

T.N. made all characterization and crystallization experiments. R.C. made all simulations. P.N. performed crystallographic analysis. Other authors were involved in developing and supervising the research.

Notes

The authors declare no competing financial interest.

■ ACKNOWLEDGMENTS

This work was financially supported by the Vidyasirimedhi Institute of Science and Technology (VISTEC) and Thailand Science Research and Innovation (TSRI), Grant FRB650023/0457.

■ REFERENCES

(1) Lorenz, H.; Czapla, F.; Polenske, D.; Elsner, M.; Seidel-Morgenstern, A. Crystallization based separation of enantiomers. *J. Chem. Technol. Metall.* **2007**, *42*, 5−16.

(2) Srimahaprom, W.; Flood, A. E. Crystal growth rates and optical resolution of dl-methionine hydrochloride by preferential crystallization from aqueous solution. *J. Cryst. Growth* **2013**, *362*, 88−92.

(3) Kongsamai, P.; Maneedaeng, A.; Flood, C.; ter Horst, J. H.; Flood, A. E. Effect of additives on the preferential crystallization of L-asparagine monohydrate. *Eur. Phys. J.: Spec. Top.* **2017**, *226*, 823−835.

(4) Sögütoglu, L.-C.; Steendam, R. R. E.; Meekes, H.; Vlieg, E.; Rutjes, F. P. J. T. Viedma ripening: a reliable crystallisation method to reach single chirality. *Chem. Soc. Rev.* **2015**, *44*, 6723−6732.

(5) Nguyen, L. A.; He, H.; Pham-Huy, C. Chiral drugs: an overview. *Int. J. Biomed. Sci.* **2006**, *2*, 85.

(6) Song, L.; Leng, F.; Robeyns, K.; Leyssens, T. Quaternary phase diagrams as a tool for ionic cocrystallization: the case of a solid solution between a racemic and enantiopure ionic cocrystal. *CrystEngComm* **2020**, *22*, 2537−2542.

(7) Springuel, G.; Leyssens, T. Innovative Chiral Resolution Using Enantiospecific Co-Crystallization in Solution. *Cryst. Growth Des.* **2012**, *12*, 3374−3378.

(8) Springuel, G.; Robeyns, K.; Norberg, B.; Wouters, J.; Leyssens, T. Cocrystal Formation between Chiral Compounds: How Cocrystals Differ from Salts. *Cryst. Growth Des.* **2014**, *14*, 3996−4004.

(9) Hutchins, K. M. Functional materials based on molecules with hydrogen-bonding ability: applications to drug co-crystals and polymer complexes. *R. Soc. Open Sci.* **2018**, *5*, No. 180564.

(10) Harmsen, B.; Leyssens, T. Dual-Drug Chiral Resolution: Enantiospecific Cocrystallization of (S)-Ibuprofen Using Levetiracetam. *Cryst. Growth Des.* **2018**, *18*, 441−448.

(11) George, F.; Norberg, B.; Robeyns, K.; Wouters, J.; Leyssens, T. Peculiar Case of Levetiracetam and Etiracetam α-Ketoglutaric Acid Cocrystals: Obtaining a Stable Conglomerate of Etiracetam. *Cryst. Growth Des.* **2016**, *16*, 5273−5282.

(12) Rémi, C.; Lorenzl, S.; Vyhnalek, B.; Rastorfer, K.; Feddersen, B. Continuous subcutaneous use of levetiracetam: a retrospective review of tolerability and clinical effects. *J. Pain Palliative Care Pharmacother.* **2014**, *28*, 371−377.

(13) Gouliaev, A. H.; Senning, A. Piracetam and other structurally related nootropics. *Brain Res. Rev.* **1994**, *19*, 180−222.

(14) Kaminski, R. M.; Matagne, A.; Patsalos, P. N.; Klitgaard, H. Benefit of combination therapy in epilepsy: a review of the preclinical evidence with levetiracetam. *Epilepsia* **2009**, *50*, 387−397.

(15) Shemchuk, O.; Song, L.; Robeyns, K.; Braga, D.; Grepioni, F.; Leyssens, T. Solid-state chiral resolution mediated by stoichiometry: crystallizing etiracetam with ZnCl2. *Chem. Commun.* **2018**, *54*, 10890−10892.

(16) Springuel, G.; Norberg, B.; Robeyns, K.; Wouters, J.; Leyssens, T. Advances in Pharmaceutical Co-crystal Screening: Effective Co-crystal Screening through Structural Resemblance. *Cryst. Growth Des.* **2012**, *12*, 475−484.

(17) Wang, J.; Peng, Y. Resolution of Halogenated Mandelic Acids through Enantiospecific Co-Crystallization with Levetiracetam. *Molecules* **2021**, *26*, 5536.

(18) Karagianni, A.; Malamatari, M.; Kachrimanis, K. Pharmaceutical Cocrystals: New Solid Phase Modification Approaches for the Formulation of APIs. *Pharmaceutics* **2018**, *10*, 18.

(19) He, Q.; Rohani, S.; Zhu, J.; Gomaa, H. Crystallization of the Racemic Compound and Conglomerate of (RS)-2-Chloromandelic Acid. *Cryst. Growth Des.* **2010**, *10*, 5136−5145.

(20) Springuel, G.; Collard, L.; Leyssens, T. Ternary and quaternary phase diagrams: key tools for chiral resolution through solution cocrystallization. *CrystEngComm* **2013**, *15*, 7951−7958.

(21) Li, S.; Liu, Y.; Yin, F.; Ye, X. Solubility Measurement and Thermodynamic Properties of Levetiracetam in Pure and Mixed Solvents. *J. Chem. Eng. Data* **2018**, *63*, 4669−4681.
(22) Gilks, S. E.; Davey, R. J.; Mughal, R. K.; Sadiq, G.; Black, L. Crystallization of 2-Chloromandelic Acid: Solubility, Formation of the Metastable Conglomerate, and Use of a Nonaqueous Emulsion To Prepare an Enantiomerically Enriched Product. *Cryst. Growth Des.* **2013**, *13*, 4323−4329.
(23) Case, D. H.; Campbell, J. E.; Bygrave, P. J.; Day, G. M. Convergence properties of crystal structure prediction by quasi-random sampling. *J. Chem. Theory Comput.* **2016**, *12*, 910−924.
(24) Tobiason, F. L.; Vergoten, G. GMMX Conformation Searching and Prediction of NMR Proton-Proton Coupling Constants. In *Biomolecular Structure and Dynamics* Vergoten, G.; Theophanides, T., Eds.; Springer Netherlands: Dordrecht, 1997; pp 179−186.
(25) Kevin, E. *Pcmodel*; Serena Software: Bloomington, IN, 2013.
(26) Halgren, T. A. Merck molecular force field. I. Basis, form, scope, parameterization, and performance of MMFF94. *J. Comput. Chem.* **1996**, *17*, 490−519.
(27) Fredericks, S.; Parrish, K. D.; Sayre, D.; Zhu, Q. PyXtal: A Python library for crystal structure generation and symmetry analysis. *Comput. Phys. Commun.* **2021**, *261*, No. 107810.
(28) Grothe, E.; Meekes, H.; de Gelder, R. Chirality and stereoisomerism of organic multicomponent crystals in the CSD. *CrystEngComm* **2020**, *22*, 7380−7388.
(29) Stewart, J. J. P. Optimization of parameters for semiempirical methods VI: more modifications to the NDDO approximations and re-optimization of parameters. *J. Mol. Model.* **2013**, *19*, 1.
(30) Gieseking, R. L. M. A new release of MOPAC incorporating the INDO/S semiempirical model with CI excited states. *J. Comput. Chem.* **2021**, *42*, 365−378.
(31) Fomin, V. N.; Gogol, D. B.; Rozhkovoy, I. E.; Ponomarev, D. L. Quantum chemical and thermodynamic calculations of fulvic and humic copper complexes in reactions of malachite and azurite formation. *Appl. Geochem.* **2017**, *79*, 9−16.
(32) Rocha-Santos, A.; Chaves, E. J. F.; Grillo, I. B.; de Freitas, A. S.; Araújo, D. A. M.; Rocha, G. B. Thermochemical and Quantum Descriptor Calculations for Gaining Insight into Ricin Toxin A (RTA) Inhibitors. *ACS Omega* **2021**, *6*, 8764−8777.
(33) Kühne, T. D.; Iannuzzi, M.; Del Ben, M.; Rybkin, V. V.; Seewald, P.; Stein, F.; Laino, T.; Khaliullin, R. Z.; Schütt, O.; Schiffmann, F.; et al. CP2K: An electronic structure and molecular dynamics software package-Quickstep: Efficient and accurate electronic structure calculations. *J. Chem. Phys.* **2020**, *152*, No. 194103.
(34) Perdew, J. P.; Burke, K.; Ernzerhof, M. Generalized gradient approximation made simple. *Phys. Rev. Lett.* **1996**, *77*, 3865−3868.
(35) Grimme, S. Density functional theory with London dispersion corrections. *Wiley Interdiscip. Rev. Comput. Mol. Sci.* **2011**, *1*, 211−228.
(36) Goedecker, S.; Teter, M.; Hutter, J. Separable dual-space Gaussian pseudopotentials. *Phys. Rev. B* **1996**, *54*, 1703−1710.
(37) VandeVondele, J.; Hutter, J. Gaussian basis sets for accurate calculations on molecular systems in gas and condensed phases. *J. Chem. Phys.* **2007**, *127*, No. 114105.
(38) Nawi, N. M.; Ransing, M. R.; Ransing, R. S. In *An Improved Learning Algorithm Based on The Broyden-Fletcher-Goldfarb-Shanno (BFGS) Method For Back Propagation Neural Networks*. Sixth International Conference on Intelligent Systems Design and Applications, 2006; pp 152−157.
(39) Ghysels, A.; Verstraelen, T.; Hemelsoet, K.; Waroquier, M.; Van Speybroeck, V. TAMkin: A Versatile Package for Vibrational Analysis and Chemical Kinetics. *J. Chem. Inf. Model.* **2010**, *50*, 1736−1750.
(40) Karimi-Jafari, M.; Padrela, L.; Walker, G. M.; Croker, D. M. Creating Cocrystals: A Review of Pharmaceutical Cocrystal Preparation Routes and Applications. *Cryst. Growth Des.* **2018**, *18*, 6370−6387.
(41) Crowley, K. J.; Zografi, G. Cryogenic grinding of indomethacin polymorphs and solvates: assessment of amorphous phase formation and amorphous phase physical stability. *J. Pharm. Sci.* **2002**, *91*, 492−507.
(42) Spackman, P. R.; Turner, M. J.; McKinnon, J. J.; Wolff, S. K.; Grimwood, D. J.; Jayatilaka, D.; Spackman, M. A. CrystalExplorer: a program for Hirshfeld surface analysis, visualization and quantitative analysis of molecular crystals. *J. Appl. Crystallogr.* **2021**, *54*, 1006−1011.
(43) Dean, P. M.; Pringle, J. M.; Forsyth, C. M.; Scott, J. L.; MacFarlane, D. R. Interactions in bisamide ionic liquids—insights from a Hirshfeld surface analysis of their crystalline states. *New J. Chem.* **2008**, *32*, 2121−2126.
(44) Zhao, Y.; Li, J.; Gu, H.; Wei, D.; Xu, Y.-c.; Fu, W.; Yu, Z. Conformational Preferences of $\pi-\pi$ Stacking Between Ligand and Protein, Analysis Derived from Crystal Structure Data Geometric Preference of $\pi-\pi$ Interaction. *Interdiscip. Sci. Comput. Life Sci.* **2015**, *7*, 211−220.
(45) Sinnokrot, M. O.; Valeev, E. F.; Sherrill, C. D. Estimates of the Ab Initio Limit for $\pi-\pi$ Interactions: The Benzene Dimer. *J. Am. Chem. Soc.* **2002**, *124*, 10887−10893.
(46) Nishio, M. The CH/π hydrogen bond in chemistry. Conformation, supramolecules, optical resolution and interactions involving carbohydrates. *Phys. Chem. Chem. Phys.* **2011**, *13*, 13873−13900.
(47) Spek, A. L. Single-crystal structure validation with the program PLATON. *J. Appl. Crystallogr.* **2003**, *36*, 7−13.
(48) Macrae, C. F.; Sovago, I.; Cottrell, S. J.; Galek, P. T. A.; McCabe, P.; Pidcock, E.; Platings, M.; Shields, G. P.; Stevens, J. S.; Towler, M.; Wood, P. A. Mercury 4.0: from visualization to analysis, design and prediction. *J. Appl. Crystallogr.* **2020**, *53*, 226−235.
(49) Herman, C.; Vermylen, V.; Norberg, B.; Wouters, J.; Leyssens, T. The importance of screening solid-state phases of a racemic modification of a chiral drug: thermodynamic and structural characterization of solid-state phases of etiracetam. *Acta Crystallogr., B: Struct. Sci. Cryst. Eng. Mater.* **2013**, *69*, 371−378.

https://doi.org/10.1021/acsomega.2c01165
ACS Omega 2022, 7, 19465−19473